BIOPHYSICS

Adaptive sampling–based structural prediction reveals opening of a $GABA_A$ receptor through the αβ interface

Nandan Haloi[1], Samuel Eriksson Lidbrink[2], Rebecca J. Howard[1,2], Erik Lindahl[1,2]*

γ-Aminobutyric acid type A ($GABA_A$) receptors are ligand-gated ion channels in the central nervous system with largely inhibitory function. Despite being a target for drugs including general anesthetics and benzodiazepines, experimental structures have yet to capture an open state of classical synaptic α1β2γ2 $GABA_A$ receptors. Here, we use a goal-oriented adaptive sampling strategy in molecular dynamics simulations followed by Markov state modeling to capture an energetically stable putative open state of the receptor. The model conducts chloride ions with comparable conductance as in electrophysiology measurements. Relative to experimental structures, our open model is relatively expanded at both the cytoplasmic (−2′) and central (9′) gates, coordinated with distinctive rearrangements at the transmembrane αβ subunit interface. Consistent with previous experiments, targeted substitutions disrupting interactions at this interface slowed the open-to-desensitized transition rate. This work demonstrates the capacity of advanced simulation techniques to investigate a computationally and experimentally plausible functionally critical of a complex membrane protein yet to be resolved by experimental methods.

INTRODUCTION

γ-Aminobutyric acid type A ($GABA_A$) receptors are pentameric ligand-gated ion channels that mediate fast inhibitory synaptic transmission in the vertebrate central nervous system. The neurotransmitter GABA, upon release at the synaptic cleft, binds to the extracellular domain (ECD) of these receptors in the resting-closed state. This triggers an allosteric signal to the transmembrane domain (TMD) to transiently open the pore for the selective flow of chloride ions across the plasma membrane, before the channel enters a desensitized state refractory to activation upon sustained GABA binding (Fig. 1A). This process is proposed to be regulated by a "dual gate mechanism": (i) The upper half of the pore, 9′ gate, is shut in the resting state; (ii) upon activation, the contraction and the rotation of the ECD ("unblooming" and "twisting") widens the 9′ gate and opens the pore; and then (iii) a gate located at the intracellular end of the pore, −2′ gate, closes during desensitization (Fig. 1B) (*1*).

Nineteen human $GABA_A$ subunits have been identified so far including α1–6, β1–3, γ1–3, δ, ε, θ, π, and ρ1–3 (*2*–*4*). In the brain, most $GABA_A$ receptors exist as heteropentamers that contain two α and two β subunits and either one γ or one δ subunit. Mainly due to this heterogeneity, a diverse set of ligands, including anesthetics such as propofol and etomidate and benzodiazepines such as diazepam, bind and modulate the functional characteristics of these channels (*2*–*7*).

Despite their biomedical relevance and informative structures solved by cryo–electron microscopy (cryo-EM) in apparent resting and desensitized states (*6*, *8*–*12*), structures of classic synaptic (α1β2/3γ2) $GABA_A$ receptors have yet to be clearly defined in an open state. At least in part, this lack is likely attributable to the transient nature of opening, which may persist for only milliseconds before proceeding to desensitization (*13*–*15*)—briefer than the typical preparation time of cryo-EM grids. Even with a variety of expression and reconstitution conditions and in the presence of positive modulators such as anesthetics, benzodiazepines, and neurosteroids, no reported structure of this $GABA_A$-receptor subtype contains a transmembrane pore large enough to permeate a hydrated chloride ion (Fig. 1C and figs. S1 and S2) (*6*–*12*, *16*).

Molecular dynamics (MD) simulation offers complementary approaches to explore experimentally unseen states. However, conventional MD simulations fail to capture the timescale at which these channels function. Although enhanced sampling methods may address this problem (*17*), most of these methods require predefined knowledge of reliable reaction coordinates of the underlying biological process and the application of artificial biasing force. None of these criteria were satisfied in our case due to the (i) complex heteromeric assembly of the channel and (ii) subtlety of the pore opening/closing that may differ as little as 1 Å between the open and desensitized states. To tackle these issues, a combination of adaptive sampling and Markov state modeling (MSM) has successfully been applied to exploring the protein conformational landscapes of systems such as Ebola viral protein 35 (*18*), epidermal growth factor receptor (*19*), and membrane transporters (*20*). In particular, a goal-oriented adaptive sampling method named fluctuation amplification of specific traits (FAST) (*21*) was able to successfully predict an experimentally unseen open state of the SARS-CoV-2 (severe acute respiratory syndrome coronavirus 2) spike complex (*22*). It has yet to exploit the power of such methods to study ion channel structure and function.

Here, we applied FAST to first explore regions of conformational space relevant to the opening of the pore in the TMD of the α1β2γ2 $GABA_A$ receptor. MSM analysis of all the simulation trajectories revealed an energetically metastable state with a pore wide enough to conduct hydrated Cl^- ions and recapitulate previously measured experimental conductance (Fig. 1, D and E) (*23*). Our analysis also revealed asymmetric rearrangements particularly at the αβ interface in the open model; mutant simulations targeting this interface exhibited a decrease in desensitization rate, consistent with previous electrophysiology experiments (Fig. 1F) (*15*). Our proposed open state offers testable hypotheses for $GABA_A$-receptor activation, with implications for mechanistic modeling and pharmacological development.

[1]SciLifeLab, Department of Applied Physics, KTH Royal Institute of Technology, Tomtebodävagen 23, Solna, 17165 Stockholm, Sweden. [2]SciLifeLab, Department of Biochemistry and Biophysics, Stockholm University, Tomtebodavägen 23, Solna, 17165 Stockholm, Sweden.
*Corresponding author. Email: erik.lindahl@dbb.su.se

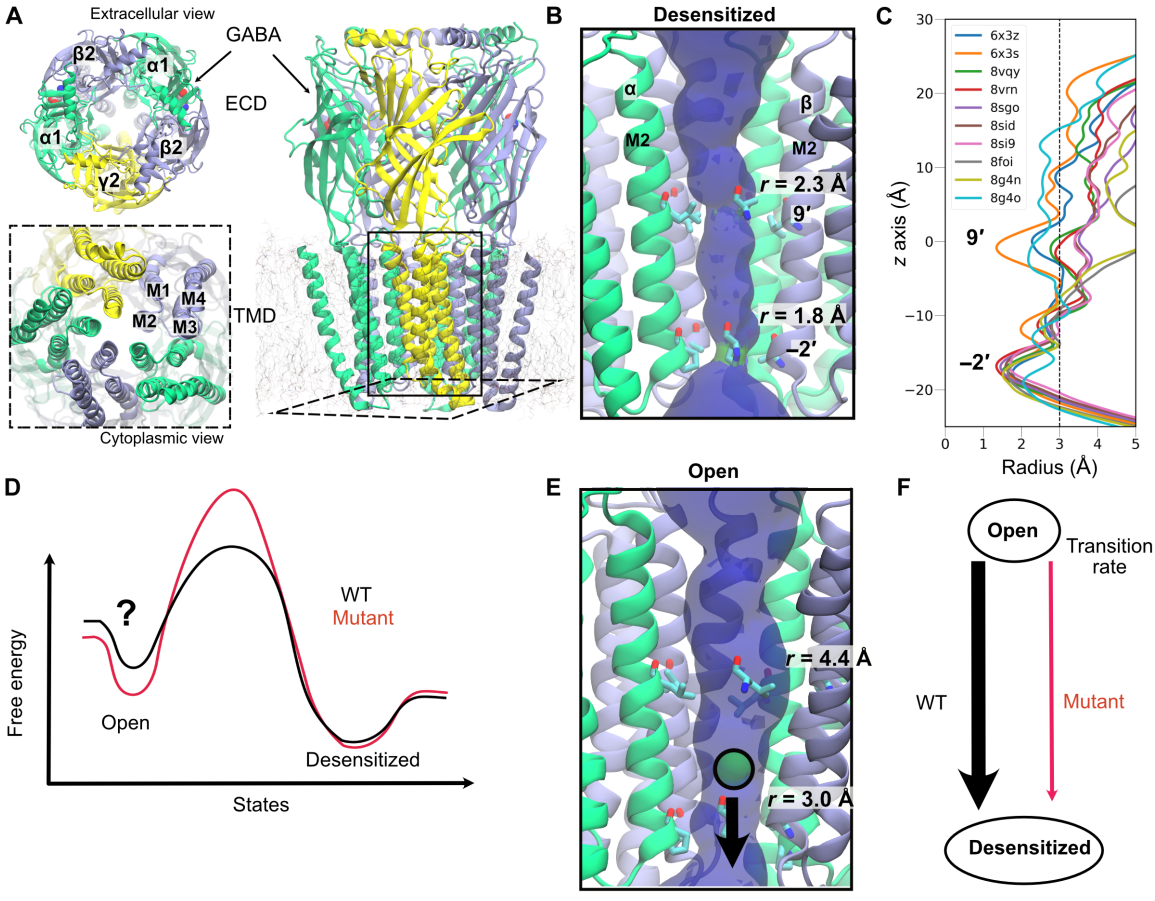

Fig. 1. Overview of structural, energetic, and kinetic aspects of $GABA_A$ receptors explored in this work. (**A**) Architecture of a $GABA_A$ receptor, colored by subunit (α in green, β in blue, and γ in yellow), viewed from the outside (left, top), cytoplasm (left, bottom), and membrane (right). In outside and membrane views, two GABA molecules at the βα interfaces are represented as van der Waals spheres. In the cytoplasm view, four helices of one β subunit are labeled. (**B**) TMD zoom view of a desensitized structure (PDB ID: 6x3z), with the γ subunit removed, colored as in (A). Surface shows the permeation pathway determined using HOLE (*63*), colored in green, where it is narrower than a water molecule. Residues at the 9′ and −2′ gates are shown as sticks, labeled by local pore radius. (**C**) Pore radius profiles of representative α1β2γ2 $GABA_A$ receptor structures from human in the presence of GABA (6x3z), bicuculline (6x3s), GABA+methaqualone (8vqy), GABA+PPTQ (8vrn), GABA+pregnenolone sulfate (8sgo), GABA+dehydroepiandrosterone sulfate (8sid), or GABA+allopregnanolone (8si9) (*6*, *8*, *64*) or from mouse in the presence of GABA+allopregnanolone (8foi), GABA+zolpidem+allopregnanolone (8g4n), or GABA+didesethylflurazepam (8g4o) (*7*). Dashed line represents the radius of a hydrated chloride ion. For additional α1β2γ2 structures reported before September 2022, see fig. S1. (**D**) Conceptually simplified free-energy profile for $GABA_A$ receptor desensitization. Lines represent WT (black) and a mutant that slows desensitization by increasing the energy barrier between open and desensitized states (red). (**E**) TMD zoom view as in (B) of the open model proposed in this study. A chloride ion (green) can readily permeate the pore. (**F**) Schematic two-state kinetic model of the WT and mutant systems studied here.

RESULTS

Adaptive sampling widens the channel pore

To maximize the chance of discovering pore openings that allow ion permeation, we launched simulations from a cryo-EM structure of the α1β2γ2 $GABA_A$ receptor determined in the presence of GABA and stabilizing Fab fragments (the latter removed in our simulation) in an apparent desensitized state [Protein Data Bank (PDB) ID: 6x3z (*8*)]. We used an adaptive sampling method, FAST, that encourages the widening of the intersubunit distances at the TMD as the MD simulations progress (see Materials and Methods for details) (Fig. 2A) (*21*). We started simulations from the desensitized state, presuming it has a similar ECD conformation as in the open state, including the agonist binding. For efficiency, our simulations were designed to capture the transition between only open and desensitized states, with the resting state presumed to contribute relatively little in the presence of an agonist. Within 30 FAST simulation generations, we observed around a twofold increase in hydration along the pore, associated with a widening of the pore (Fig. 2B).

MSM captures an energetically metastable open state

To identify key conformational states of the $GABA_A$ receptor, their underlying free-energy and kinetics of state transitions, we constructed an MSM using all the FAST-sampled MD trajectories (see Materials and Methods for details). The free energy was projected on the first two time-lagged independent components (tICs), which capture the slowest transitions of the system (*24*). The energy landscape revealed three metastable states (Fig. 2, C to E). Whereas all experimental structures determined in the presence of an agonist projected to desensitized or sheared states (described below; Fig. 2D and fig. S3), our analysis also revealed a putative open state in which both the central (9′) and intracellular (−2′) gates are wide enough to

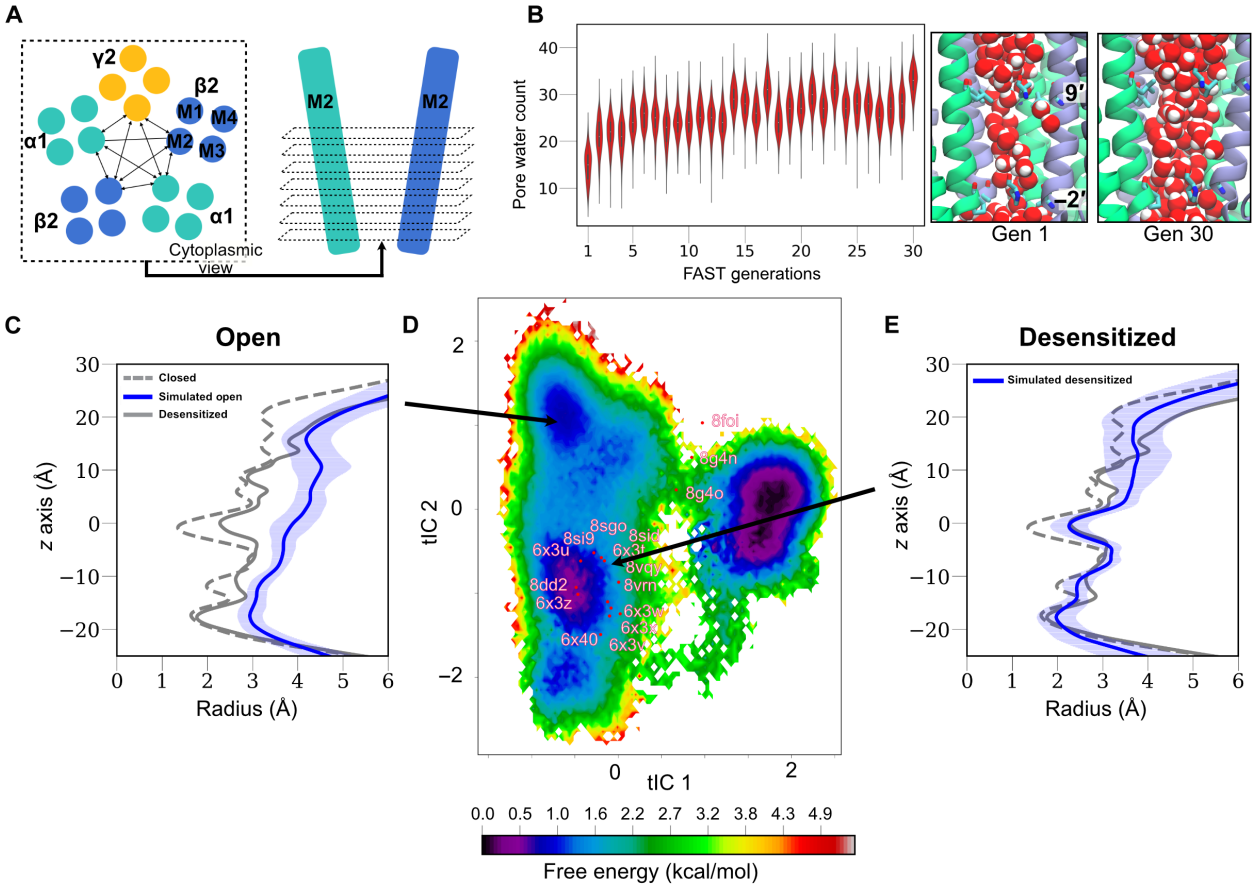

Fig. 2. Structural and energetic characterization of the $GABA_A$ receptor during our FAST sampling and MSM analysis. (**A**) Schematic depiction of the feature selection criteria for the FAST sampling. All possible combinations of pairwise distances among the M2 helix of all the subunits, spanning from the −4′ to 22′ were chosen as an input feature in FAST. (**B**) Increased water hydration, along the progression of FAST generations, characterized by counting water in between the two gates (left). A representative snapshot of water hydration in the first and last generation of FAST sampling is shown on the right. (**C** to **E**) Structural characteristics of the metastable states captured in the free-energy landscape, projected onto the top two tICA eigenvectors from our MSM. The pore radius profiles [calculated using CHAP (*65*)] with a mean (solid) and SD (shaded) are shown in blue. The pore radius profiles of experimental closed (PDB ID: 6x3s) and desensitized (PDB ID: 6x3z) state structures are shown in gray dashed line and gray solid line, respectively. The structural feature of the third metastable state (rightmost) on the free-energy landscape is shown in fig. S6.

permeate hydrated chloride ions, with average radii of ≈4 and ≈3 Å, respectively (Fig. 2C). Notably, MSM analysis showed that the open state is energetically less favorable, as expected relative to the long-lived desensitized state (Fig. 2, C and D). This notion was further supported by our computed open-state probability of 3.4%, using the first eigenvector of the transition probability matrix (TPM) in our MSM analysis. A similarly low open-state probability of around 16% was reported in previous experiments (*25*). To further check the structural stability of this open state in additional MD simulations, we performed six replicates of simulations, each for 200 ns. In five of these replicates, the pore remained stably open, as evident by the minimal pore radius persisting at 3 Å at the end of the simulations (fig. S4).

To test the dependence of our putative open state on the starting structure (GABA-bound α1β2γ2 subtype), we launched an independent set of FAST simulations followed by MSM analyses based on the structure of an α1β3γ2 $GABA_A$ receptor with GABA and alprazolam (PDB ID: 6huo). For consistency with our initial setup, all simulations were run with GABA alone as a ligand. The resulting free-energy landscape again contained a distinct well with open-like features; snapshots from this basin largely projected to the open state in our initial α1β2γ2 landscape (fig. S5).

In addition to the apparent open state, two other prominent wells were apparent in our free-energy landscapes. In one of these, pore profiles were comparable to the GABA-bound desensitized structure (PDB ID: 6x3z), with an average radius of ≈2.0 Å at the −2′ and ≈2.3 Å at the 9′ gate (Fig. 2E). We accordingly assigned this basin to the desensitized state; most desensitized experimental structures projected here (Fig. 2D and fig. S1). In the other prominent basin, the 9′ gate was relatively expanded (radius ≈ 3.0 Å), but the −2′ gate was again too narrow (radius ≈ 2.2 Å) for a hydrated chloride to pass (fig. S6). Representative models from this basin were notably asymmetrical, with three subunits collapsing inward toward the channel pore and one β subunit displacing outward. Given its asymmetry, we characterized this state as "sheared." Three recent structures from native mouse brains (*7*) projected near this basin (Fig. 2D and fig. S6). However, given the apparent lack of conductance and limited experimental evidence for this latter state, we focused our subsequent analyses on the transition from predicted open to experimental desensitized states.

Simulated conductance of the open state agrees with experimental results

To validate the functional characteristics of our open-state model, we performed electric field simulations corresponding to an electric potential difference of 200 and −200 mV across the membrane, each for six replicates. These simulations revealed a conductance of 17 ± 8.9 pS at 200 mV and 9.3 ± 5 pS at −200 mV, similar to previous electrophysiology experiments reporting conductances values of 16.6 ± 3.6 (Fig. 3A) (*23*). Note that, at 200 mV, the chloride flows inward which is the predominant direction of ionic flow in neurons. Our desensitized model exhibited virtually no conductance at either voltage, confirming the presence of a constricted gate (Fig. 3A).

We further characterized the energetics of chloride ion permeation from these two states by performing potential of mean force (PMF) calculations using the accelerated weight histogram (AWH) MD simulation method (Fig. 3B and fig. S7) (details in the Materials and Methods section) (*26*). The ion faces lower energy barriers at both gates in the open state compared to the desensitized state, consistent with the higher conductance through the former model. In the open state, the highest barrier is still around 4 kcal/mol at the −2′ gate. This is possibly due to the partial dehydration, as defined by losing one water molecule in the first hydration shell, of the ion. This loss cannot be completely compensated by uncharged residues at this location (Fig. 3, B and C).

Open model features distinctive expansion at the αβ interface

Given that our open model was primarily distinguished by pore expansion spanning the −2′ and 9′ gates (Fig. 1C), we next sought to identify specific rearrangements in proximal regions of the TMD. We first noticed that pore expansion was asymmetric: At the cytoplasmic end of the pore, the open model featured a pronounced expansion at the αβ interface, relative to closed or desensitized experimental structures (Fig. 4A). Specifically, in contrast to other subunit interfaces (fig. S8), the median distance between −2′ Cα atoms at the αβ interface was >3 Å larger in our open than in either the closed or desensitized states.

Open-state expansion in this region corresponded to increased solvent-accessible surface area (SASA) in a pocket at the αβ interface, facing the inner membrane leaflet. SASA in this pocket was >20% larger in our open model than in closed or desensitized structures (Fig. 4B). Similar trends were apparent in the α1β3γ2 system (Fig. 4 and fig. S8). An equivalent pocket at the βα interfaces was recently shown to bind the endogenous modulator allopregnanolone, both in heterologously expressed human receptors and native mouse receptors (*6*, *7*); it is interesting to consider whether the αβ interface might offer an alternative druggable site, potentially even more selective for the open versus desensitized states.

On the basis of experimental structures in closed versus desensitized states, GABA binding has also been shown to expand the αβ interface in a region facing the outer membrane leaflet (*8*). Such expansion enables state- and interface-selective binding of the barbiturate drug phenobarbital. As predicted, this pocket was also accessible to phenobarbital in our open model (fig. S9), supporting its relevance to barbiturate potentiation and the feasibility of modulation via the αβ interface. Thus, regions of the αβ interface facing both inner and outer membrane leaflets expand upon GABA activation; upon desensitization, the inner-leaflet pocket is restored to a contracted configuration (Fig. 4B), whereas the outer-leaflet pocket remains accessible to drugs (fig. S9).

We further sought to identify specific amino acid contacts that might influence distinctive rearrangements of the open state. In contrast to other interfaces (fig. S10), α-V263 (M2 position 8′) formed a >1-Å closer contact with β-V238 (M1) in our open model than in either closed or desensitized structures (Fig. 4C). This tightened interaction appeared to be coordinated with translocation of the pore-lining α-M2 helix outward from the pore (toward β-M1) upon activation and inward (toward the pore) upon desensitization. Again, similar trends were apparent in the α1β3γ2 system (Fig. 4C and fig. S10).

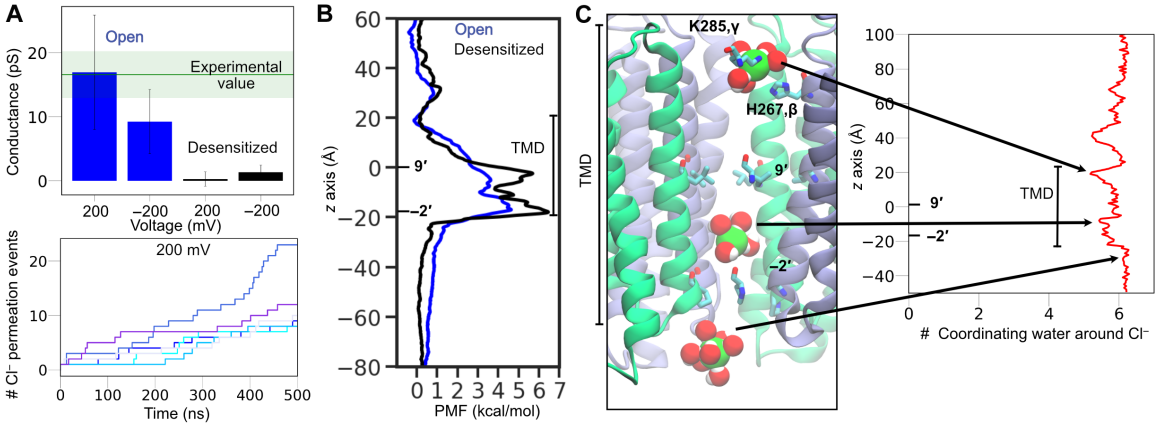

Fig. 3. Simulated conductance of the open state agrees with experimental results. (**A, top**) Mean and SD of conductance for the open (blue) and desensitized (black) states, determined using six independent electric field simulations for each state. The experimental values are depicted in a green horizontal line (*23*). (**A, bottom**) Cumulative net number of channel-crossing events by a chloride ion, tracked over the time course of six independent MD simulations (colored differently) for the open state at 200 mV. (**B**) Free energies for chloride ion permeation along the pore axis (with 9′ gate at 0 Å), for the open (blue) and desensitized state (black) of the receptor. The location of the TMD is highlighted. The convergence of the free energies can be found in fig. S7. (**C**) Water coordination at the first hydration shell of a chloride ion. Molecular snapshots at different locations of the ion are shown on the left. The water coordination number along the pore axis, calculated using all the simulation trajectories of the ion permeation free energy, is shown on the right.

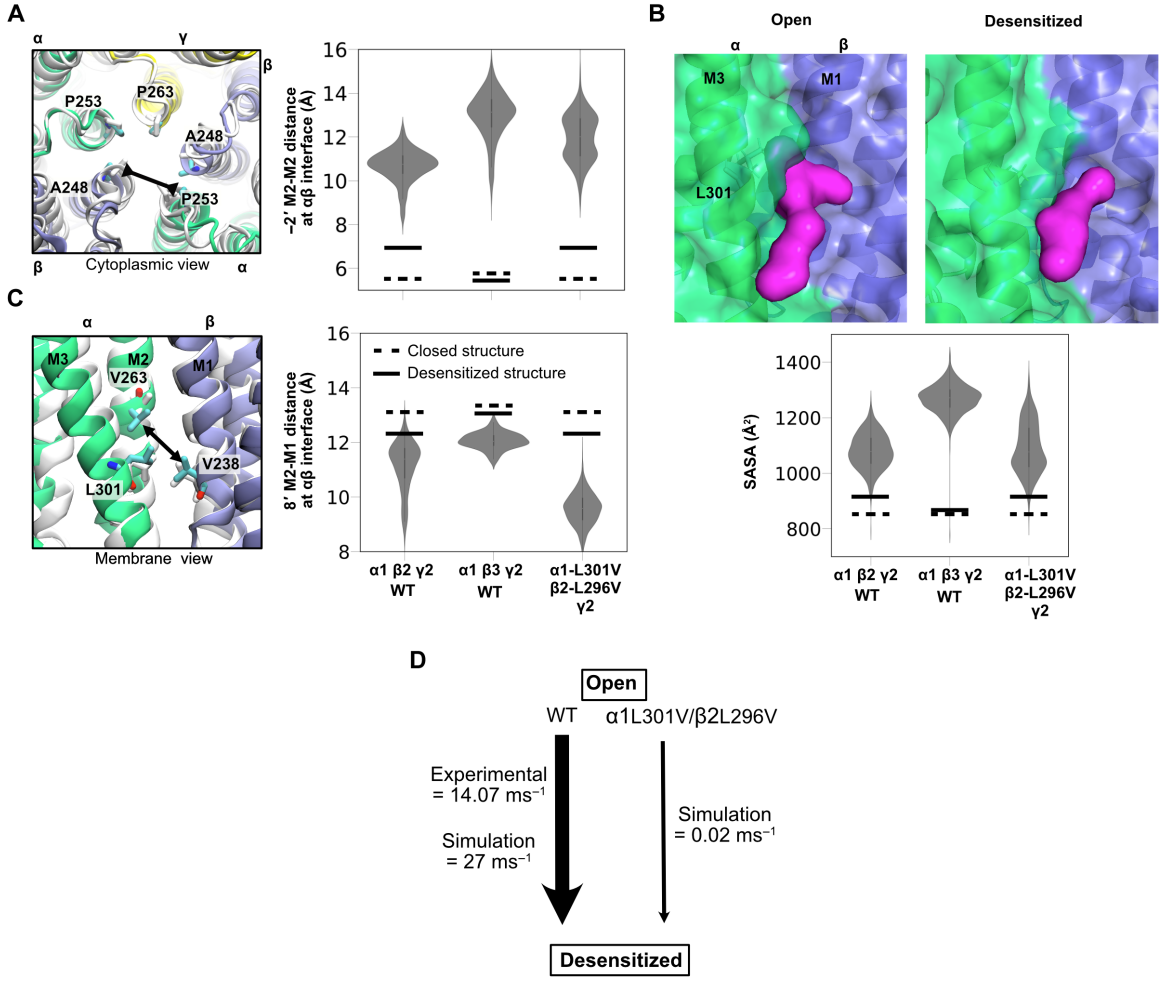

Fig. 4. Open-to-desensitized transition characterized by contraction, and slowed by mutagenesis, at the αβ interface. (**A**) Left: Zoom view of the transmembrane pore proximal to the −2′ gate, viewed from the cytoplasm, showing the open model (colored) superimposed with the desensitized structure (PDB ID: 6x3z, white) based on the entire TMD. Arrow indicates contraction between −2′ residues at the αβ interface upon desensitization. Right: Violin plots showing Cα distances between −2′ residues at the αβ interface in open models proposed for the WT-α1β2γ2, WT-α1β3γ2, and α1-L301Vβ2-L296Vγ2 (mutant) systems. Horizontal lines indicate closed (PDB ID: 6x3s, dashed) and desensitized (PDB ID: 6x3z, solid) experimental structures. (**B**) Top: Zoom views of the αβ interface in the open model (left) and desensitized structure (PDB ID: 6x3z; right), shown as cartoons with semitransparent surfaces. Magenta volumes indicate SASA, calculated in VMD based on the inner leaflet–facing halves of the principal M2-M3 and complementary M1-M2 helices. Bottom: Violin plots showing the corresponding αβ-interface SASA in open models proposed for α1β2γ2, α1β3γ2, and mutant systems. (**C**) Left: Zoom view of the TMD proximal to the 9′ gate, viewed from the membrane and colored as in (A). Arrow indicates expansion between α-V263 and β-V238 upon desensitization. Right, violin plots showing distances between Cα atoms of α-V263 and β-V238 in open models proposed for α1β2γ2, α1β3γ2, and mutant systems. (**D**) Rates for the open-to-desensitized transitions in the WT and mutant α1β2γ2 systems, calculated using the transition path theory in pyEmma (*43*), with thicker lines indicating faster rates. Experimentally derived rate for the WT system (*13*) is shown for comparison.

In silico mutagenesis slows desensitization, in accordance with experiments

We noted that mutations at a conserved leucine residue (α1-L301 and β2-L296) have been shown to decrease desensitization rates in electrophysiology measurements (*15*). Located on the principal face of the M3 helix, α-L301 faces both α-V263 and β-V238, as well as the inner-leaflet pocket described above (Fig. 2, B and C). We therefore predicted that introducing equivalent mutations in our computational pipeline would modify interfacial interactions and slow the open-to-desensitized transition.

To test this hypothesis, we used in silico mutagenesis to substitute valine at α1-L301 and β2-L296 in the GABA-bound desensitized structure [PDB ID: 6x3z (*8*)]. Then, we repeated our adaptive sampling method followed by MSM analysis to identify a mutant open model. Using transition path analysis (*27*), we calculated a desensitization timescale of 27 ms^{-1} for the wild-type (WT) system, comparable to estimates from previous electrophysiology recordings (14 ms^{-1}) (Fig. 4D and fig. S11) (*13*). Consistent with mutagenesis experiments (*15*), desensitization in the mutant system was 1000-fold slower, with a timescale of 0.02 ms^{-1}.

The open-state ensemble for the mutant system generally projected onto the open-state free-energy well in the WT landscape (fig. S5), indicating that our WT and mutant open models were convergent. Furthermore, our representative open model for the mutant receptor exhibited similar asymmetric features as for WT, including expansion of the αβ interface (Fig. 4A and fig. S8) and the

inner-leaflet pocket (Fig. 4B). Proximal to the truncated α-L301V side chain, the contact between α-V263 and β-V238 tightened even more markedly in the mutant versus WT open models (Fig. 4C and fig. S10). Although our engineered mutant also contained valine substitutions at the βα and αγ interfaces, M2-M1 contacts at those interfaces were not tightened (fig. S10), indicating that this rearrangement is specific to the αβ interface.

Limitations to artificial intelligence–based prediction of a plausible open $GABA_A$ receptor

Given the recent success of artificial intelligence–based methods such as AlphaFold (AF) in sampling divergent protein conformations (*28*–*30*), we also sought to compare our FAST/MSM-based approach to AF prediction of an open $GABA_A$ receptor. To this end, we generated 1000 α1β2γ2 $GABA_A$-receptor conformations using AF by stochastically subsampling the multiple sequence alignment (MSA) depth (see Materials and Methods for details) and screened them on the basis of pore radius and physical plausibility. Of these 1000, 8 models contained pore profiles consistent with an open $GABA_A$ receptor (radius of 2.8 to 5.0 Å across both gates) (fig. S12). However, typical AF implementations do not enable specification of subunit arrangement in heteromeric complexes; only two of these eight models featured the physiological βαβαγ arrangement, viewed counterclockwise from the extracellular side (Fig. 1A). Among these two, both contained oversized, solvent-accessible gaps at transmembrane subunit interfaces (fig. S12). Thus, AF modeling in our hands, even starting from 1000 initial conformations, has yet to predict a plausible open α1β2γ2 $GABA_A$-receptor model.

DISCUSSION

Although yet to be directly visualized by laboratory methods, the model we propose here—based on an integrative computational strategy involving adaptive sampling and Markov-state modeling—satisfies several key conditions for the elusive open-state α1β2γ2 $GABA_A$ receptor. Our model contains a fully hydrated pore and conducts chloride ions to a similar extent as in electrophysiology experiments (Fig. 3A) (*23*). It is also representative of a free-energy basin (Fig. 2D), metastable in extended simulations (fig. S4), and largely reproducible from multiple starting structures (fig. S5). Relative to the desensitized state, it features rearrangements in a druggable pocket at the transmembrane subunit interface, where mutations have also been shown to decrease desensitization rates (*15*). This model may therefore prove applicable to developing mechanistic hypotheses as well as pharmacological or therapeutic tools.

On the basis of our open model, receptor activation and desensitization were associated with expansion and contraction (respectively) throughout the transmembrane pore, spanning the −2′ and 9′ gates (fig. S13). This mechanism may highlight a fundamental complexity of the "dual gate" model, which—in more simplistic terms—associates activation with expansion around 9′ and desensitization with contraction at −2′ (*1*). Although no open structure has been reported for the classical synaptic human $GABA_A$ receptor, related receptors for glycine (*31*) and acetylcholine (*32*) are now available in apparent closed, open, and desensitized states, enabling more detailed mechanistic modeling. These family members exhibit similar patterns of expansion and contraction spanning both gates (fig. S13), indicating that it may be a generalized feature. Still, we note that the present work focuses on predicting a plausible open state; it does not resolve a complete gating mechanism of $GABA_A$-receptor function, which would include additional functional states and their precise interconversion pathways. For instance, the complex coupling of pore opening to ECD-ligand binding in the closed-to-open transition remains of critical interest to past and future studies.

Our open model did reveal distinctive rearrangements at the αβ interface associated with channel gating (Fig. 5). Open-state expansion between neighboring α-M2 and β-M2 helices, particularly around −2′ (Fig. 4A), was coordinated with tightened contacts between α-M2 and β-M1 (Fig. 4C). Tightening this M2-M1 contact even further (in the presence of α-L301V) was associated with slower desensitization, i.e., a heightened free-energy cost to disrupting open-state contacts (Fig. 4D). Notably, a similarly tightened M2-M1 contact has been described as a key feature of gating in other pentameric ligand-gated ion channels (*33*). This feature may support translocation of M2 away from the channel pore or even local distortion of M2 helices, as reported recently for the open α7 nicotinic receptor (*34*).

On the basis of our open model, receptor activation is further associated with the evolution of two types of intersubunit pockets, particularly at the αβ interface (Fig. 5). A pocket facing the outer membrane leaflet is relatively expanded in both open and desensitized states, enabling it to bind positive allosteric modulators such as phenobarbital (fig. S9) (*8*). A pocket facing the inner membrane leaflet expands upon GABA activation and then contracts upon desensitization (Fig. 4B). To our knowledge, the pocket has yet to be implicated in binding any known modulators, suggesting a pathway for pharmacological development.

In addition to mechanistic details, our study provides thermodynamic and kinetic measures of channel function that can be compared to experiential findings. As seen in Fig. 2D, the free energy of the open state is relatively high, corresponding to an open probability of 3.4%, reminiscent of experimental values of 16% (*25*). Our transition path analysis shows that the receptor desensitizes from the open state with a rate of around 27 ms^{-1}, qualitatively agreeing with values from single-channel recordings of 14.07 ms^{-1} (*13*). Although not perfectly precise, such measures offer benchmarks for further refinement of structural and mechanistic models.

Given that the free-energy basin for the sheared state was lower than other states, we were initially surprised that such a conformation had yet to be described in the experimental literature. It is possible that sheared-state particles are not readily extracted from cryo-EM data by class averaging and/or that its prominence in our free-energy landscapes is biased by limited sampling using the FAST method. Although this was anticipated in our experimental design, our simulations excluded sampling of the closed state, as indicated by the absence of any free-energy well corresponding to the 9′ radius of closed experimental structures (1.2 Å, Fig. 1C).

Subsequent to the initiation of this work, three α1β2γ2 $GABA_A$ receptor structures were reported (*7*), which did approach the sheared state in our free-energy landscape (fig. S6). Derived from native mouse brains, these structures were resolved with endogenous ligands including GABA and allopregnanolone (*7*), enabling direct comparison to recombinant human variants resolved under equivalent conditions. Relative to a comparable human structure [PDB ID: 8si9 (*6*)] that projected to the desensitized state, the mouse structure [PDB ID: 8foi (*7*)] exhibited inward collapse of at least three subunits around the −2′ gate (fig. S14), similar to our representative sheared model (fig. S6). Although it remains unclear whether these differences are primarily attributable to species, expression system, or other physiological or experimental variations,

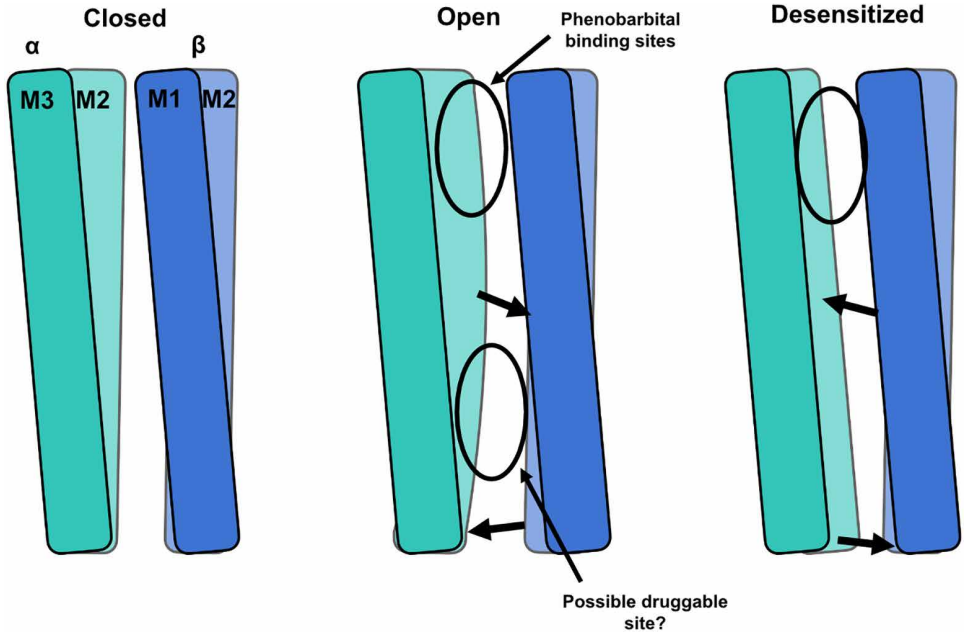

Fig. 5. Graphical overview of $GABA_A$ receptor open-state transitions at the αβ interface as proposed in this study. (**Left**) View from the membrane plane of the interface between M2-M3 of an α subunit (green) and M1-M2 of a β subunit (blue) in the resting-closed state. (**Middle**) Rearrangements upon pore opening expand the interface between α-M2 and β-M2 helices (bottom arrow). In conjunction with these rearrangements, the α-M2 helix displaces outward from the pore toward β-M1 (middle arrow). These motions are associated with the evolution of lipid-accessible pockets facing the outer and inner membrane leaflets (circles). (**Right**) Rearrangements upon desensitization partially release contacts between α-M2 and β-M1 (middle arrow) and restore closer contacts between α-M2 and β-M2 helices (bottom arrow). Whereas the outer-leaflet pocket remains accessible to phenobarbital in the desensitized state, the inner-leaflet pocket appears to be specific to the open state and may constitute a druggable site to promote channel opening.

the observation expands experimental sampling of the conformational landscape and supports the potential relevance of a sheared-like state.

Overall, this study demonstrates the power of advanced sampling strategies and MSM analysis that can be used to address challenging biological questions. Given the fact that we did not use information on the open state from a homologous protein, this method appears to be a promising approach for sampling the conformational landscape of a range of proteins lacking mechanistic detail, in particular to propose testable models for previously unidentified functional states of ion channels and drive prospective pharmacological development.

MATERIALS AND METHODS

System preparations

Initial simulations were launched from a cryo-EM structure of an α1β2γ2 $GABA_A$ receptor in a GABA-bound desensitized state (PDB ID: 6x3z). For consistency with a past work, we used a simulation system previously embedded and equilibrated in a model membrane using coarse-grained methods; for details, see ref. (*8*). Briefly, the experimental structure was coarse-grained through the representation of about four heavy atoms as a single bead, using Martini Bilayer Maker in CHARMM-GUI (*35*). Then, the protein was embedded in a symmetric membrane containing 44.4% cholesterol, 22.2% POPC (1-palmitoyl-2-oleoyl-*sn*-glycero-3-phosphocholine), 22.2% POPE (1-palmitoyl-2-oleoyl-*sn*-glycero-3-phosphoethanolamine), 10% POPS (1-palmitoyl-2-oleoyl-*sn*-glycero-3-phospho-L-serine), and 1.1% PtdIns(4,5)P2 (phosphatidylinositol 4,5-bisphosphate), previously shown to approximate the neuronal plasma membrane (*36*). Following 20-μs equilibration, this coarse-grained system was backmapped to an all-atom system, solvated with transferable intermolecular potential with 3 points (TIP3P) water (*37*) and neutralized with 0.15 M NaCl, resulting in a system containing 270,000 atoms with dimensions of 140 by 140 by 160 $Å^3$.

For simulations of the α1β3γ2 $GABA_A$ receptor, for which no structure was readily available with GABA alone, we used a cryo-EM structure with GABA+alprazolam (PDB ID: 6huo) (*11*), with alprazolam removed. As an alternative to coarse-grained equilibration of the membrane, we constructed the initial generation of FAST sampling (described in detail below) from 25 independent replicas built by randomly configuring initial lipid placement around the GABA-protein complex using the Membrane mixer plugin in VMD (*38*, *39*).

The systems were energy minimized and then relaxed in simulations at constant pressure (1 bar) and temperature (310 K) for 30 ns, during which the position restraints on the protein and GABA were gradually released. The restraints were directly used as recommended by CHARMM-GUI. Then, production runs were performed with a mild flat-bottom restraint of 20 kJ mol^{-1} nm^{-2} between the atoms of GABA and residues at the binding sites to prevent spontaneous release of GABA from the binding sites as seen in a previous study (*8*).

Adaptive sampling

To explore pore opening in the TMD, we applied the FAST goal-oriented adaptive sampling method (*21*). Briefly, this method runs successive swarms of simulations where the starting points for each swarm are chosen from the set of all previously found conformations based on a reward function. This function balances (i)

preferentially simulating structures with maximum pairwise distances (with a total of 540 pairs; Fig. 2A) to encourage the pore to adopt a more open conformation that may allow ion permeation, with (ii) broadly exploring of the conformational space of the entire receptor. The broad exploration phase was implemented by favoring states that are poorly sampled compared to other states, based on the root mean square deviation of the TMD residues. During FAST, we performed 30 generations of simulations with 25 simulations per generation and 40 ns per simulation, totaling to 30 μs. Because no biasing force is applied to any individual simulation, the final dataset can be used to build an MSM to extract thermodynamic and kinetic properties (*40*–*42*), as detailed below.

Markov state modeling

We used our trajectory dataset from FAST to construct an MSM using pyEmma (*43*), by first featurizing the trajectory dataset using (i) the pore radii, spanning from −2′ to 9′, every 1 Å, and (ii) M2-M2 intersubunit distances and M2-M1 and M2- M3 intrasubunit distances spanning the same region as above. To remove redundant information within the feature space and identify the slowest reaction coordinates, time-structure–based independent component analysis (tICA) was used to reduce the dimensionality of the feature space $[X(t)]$ to the eigenvectors of an autocovariance matrix, $\langle X(t)X^T(t+\tau)\rangle$, with a lag time, $\tau = 1$ ns (*24*, *44*, *45*). It is important to choose an optimal number of tICA eigenvectors because an MSM built using too many eigenvectors would have microstates with low statistical significance due to finite sampling error (*46*). We found that the first 12 tICA eigenvectors are sufficient to construct the MSM, as assessed by the convergence of the VAMP-2 score (fig. S15) (*47*).

The conformational space was then discretized into multiple microstates using *k*- means clustering. To choose the number of microstates to use in the model, we used the VAMP-2 score (*47*) to evaluate the quality of MSMs built with different numbers of microstates (fig. S15).

Then, a TPM was constructed by evaluating the probability of transitioning between each microstate within a lag time, τ. To choose an adequate lag time to construct a TPM that ensures Markovian behavior, multiple TPMs were first created using multiple maximum likelihood MSMs with different lag times. The implied timescales were evaluated for each of these transition matrices, and saturation was observed at $\tau = 5$ ns for the WT and $\tau = 8$ ns for the mutant system (fig. S16). Thus, we built our final TPM using a maximum likelihood MSM with the corresponding lag times. This final TPM is symmetrized using a maximum likelihood approach to ensure detailed balance (*43*). Convergence was verified in pyEMMA using Chapman-Kolmogorov tests (*48*) for each system (figs. S17 to S19).

MD simulations

MD simulations in this study were performed using GROMACS-2023 (*49*) using CHARMM36m (*50*) and CHARMM36 (*51*) force field parameters for proteins and lipids, respectively. The force field parameters for the ligands were generated using the CHARMM General Force Field (*52*–*54*). Cation-π interaction-specific NBFIX parameters were used to maintain appropriate ligand-protein interactions at the aromatic cage, located at the binding sites (*55*). Bonded and short-range nonbonded interactions were calculated every 2 fs, and periodic boundary conditions were used in all three dimensions. The particle mesh Ewald method (*56*) was used to calculate long-range electrostatic interactions with a grid density of 0.1 nm^{-3}. A force-based smoothing function was used for pairwise nonbonded interactions at 1 nm with a cutoff of 1.2 nm. Pairs of atoms whose interactions were evaluated were searched and updated every 20 steps. A cutoff of 1.2 nm was applied to search for the interacting atom pairs. Constant pressure was maintained at 1 bar using the Parrinello-Rahman algorithm (*57*). Temperature coupling was kept at 300 K with the *v*-rescale algorithm (*58*).

Ion permeation free-energy calculations

The free energy along the pore axis for chloride was calculated using the AWH method (*26*). In brief, for each structural model of open and desensitized state captured in our MSM analysis, we applied one independent AWH bias and simulated for 500 ns each with eight walkers sharing bias data and contributing to the same target distribution. Each bias acts on the center-of-mass *z*-distance between one central chloride ion and the −2′ residues, with a sampling interval across more than 95% of the box length along the *z* axis to reach periodicity. To keep the solute close to the pore entrance, the coordinate radial distance was restrained to stay below 10 Å by adding a flat-bottom umbrella potential. During these simulations, the protein-heavy atoms were harmonically restrained using a relatively weak force constant of 100 kJ mol^{-1} $Å^{-2}$ to the backbone atoms to maintain the respective conformational state of the protein.

Electric field simulations

Ionic current was calculated by performing simulations with a constant electric field normal to the membrane. Six replicas of ionic current simulations were performed with an open and desensitized state $GABA_A$ receptor model, derived from MSM analysis. Each production simulation was then performed for 500 ns with an electric field corresponding to a membrane electric potential difference of 200 and −200 mV. During these simulations, the protein-heavy atoms were harmonically restrained using a relatively weak force constant of 100 kJ mol^{-1} $Å^{-2}$ to the backbone and 20 kJ mol^{-1} $Å^{-2}$ to the side-chain atoms to maintain the respective conformational state of the protein.

Ionic current (*I*) was computed by counting the number of ions (Na^+ and Cl^-) that cross the pore over time, i.e., $I = N \times q/\tau$, where *N* is the number of ion crossing events over a time interval τ, and *q* is the charge of the ion ($1.60217662 \times 10^{-19}$ C for Na^+ and $-1.60217662 \times 10^{-19}$ C for Cl^-). The total current was simply the sum of the net Na^+ current minus the net Cl^- current. The conductance (*C*) was then calculated as $C = I/V$.

AF sampling

AlphaFold2 conformations were generated by running AlphaFold-Multimer (*59*) in ColabFold (*60*), where all the MSAs are obtained from the MMseqs2 database (*61*). The MSA depth was subsampled according to methods proposed by del Alamo *et al.* (*28*), using a single recycle and no energy minimization. The sequence number parameters were selected by initially generating conformations with *max-extra-seq* = 100, 120, . . ., 380, 400 and *max-seq* = *max-extra-seq*/2 using all five different AlphaFold-Multimer models (*num-models* = 5), resulting in a total of 1000 conformations.

Statistical analysis

System visualization and analysis were carried out either using VMD (*39*) or PyMOL (*62*). Violin plots were prepared in Python using seaborn.violinplot with default settings.

Supplementary Materials

This PDF file includes:

Figs. S1 to S19
References

REFERENCES AND NOTES

1. M. Gielen, P.-J. Corringer, The dual-gate model for pentameric ligand-gated ion channels activation and desensitization. *J. Physiol.* **596**, 1873–1902 (2018).
2. W. Sieghart, M. M. Savić, International Union of Basic and Clinical Pharmacology. CVI: $GABA_A$ receptor subtype-and function-selective ligands: Key issues in translation to humans. *Pharmacol. Rev.* **70**, 836–878 (2018).
3. E. Sigel, M. Ernst, The benzodiazepine binding sites of $GABA_A$ receptors. *Trends Pharmacol. Sci.* **39**, 659–671 (2018).
4. R. W. Olsen, $GABA_A$ receptor: Positive and negative allosteric modulators. *Neuropharmacology* **136**, 10–22 (2018).
5. J. J. Kim, R. E. Hibbs, Direct structural insights into $GABA_A$ receptor pharmacology. *Trends Biochem. Sci.* **46**, 502–517 (2021).
6. D. H. Legesse, C. Fan, J. Teng, Y. Zhuang, R. J. Howard, C. M. Noviello, E. Lindahl, R. E. Hibbs, Structural insights into opposing actions of neurosteroids on $GABA_A$ receptors. *Nat. Commun.* **14**, 5091 (2023).
7. C. Sun, H. Zhu, S. Clark, E. Gouaux, Cryo-EM structures reveal native $GABA_A$ receptor assemblies and pharmacology. *Nature* **622**, 195–201 (2023).
8. J. J. Kim, A. Gharpure, J. Teng, Y. Zhuang, R. J. Howard, S. Zhu, C. M. Noviello, R. M. Walsh Jr., E. Lindahl, R. E. Hibbs, Shared structural mechanisms of general anaesthetics and benzodiazepines. *Nature* **585**, 303–308 (2020).
9. S. Phulera, H. Zhu, J. Yu, D. P. Claxton, N. Yoder, C. Yoshioka, E. Gouaux, Cryo-EM structure of the benzodiazepine-sensitive $\alpha1\beta1\gamma2s$ tri-heteromeric $GABA_A$ receptor in complex with GABA. *eLife* **7**, e39383 (2018).
10. S. Zhu, C. M. Noviello, J. Teng, R. M. Walsh Jr., J. J. Kim, R. E. Hibbs, Structure of a human synaptic $GABA_A$ receptor. *Nature* **559**, 67–72 (2018).
11. S. Masiulis, R. Desai, T. Uchański, I. Serna Martin, D. Laverty, D. Karia, T. Malinauskas, J. Zivanov, E. Pardon, A. Kotecha, J. Steyaert, K. W. Miller, A. R. Aricescu, $GABA_A$ receptor signalling mechanisms revealed by structural pharmacology. *Nature* **565**, 454–459 (2019).
12. D. Laverty, R. Desai, T. Uchański, S. Masiulis, W. J. Stec, T. Malinauskas, J. Zivanov, E. Pardon, J. Steyaert, K. W. Miller, A. R. Aricescu, Cryo-EM structure of the human $\alpha1\beta3\gamma2$ $GABA_A$ receptor in a lipid bilayer. *Nature* **565**, 516–520 (2019).
13. M. Jatczak-Śliwa, K. Terejko, M. Brodzki, M. A. Michalowski, M. M. Czyzewska, J. M. Nowicka, A. Andrzejczak, R. Srinivasan, J. W. Mozrzymas, Distinct modulation of spontaneous and GABA-evoked gating by flurazepam shapes cross-talk between agonist-free and liganded $GABA_A$ receptor activity. *Front. Cell. Neurosci.* **12**, 237 (2018).
14. P. T. Kaczor, A. D. Wolska, J. W. Mozrzymas, $\alpha1$ subunit histidine 55 at the interface between extracellular and transmembrane domains affects preactivation and desensitization of the $GABA_A$ receptor. *ACS Chem. Nerosci.* **12**, 562–572 (2021).
15. M. Gielen, P. Thomas, T. G. Smart, The desensitization gate of inhibitory Cys-loop receptors. *Nat. Commun.* **6**, 6829 (2015).
16. A. Sente, R. Desai, K. Naydenova, T. Malinauskas, Y. Jounaidi, J. Miehling, X. Zhou, S. Masiulis, S. W. Hardwick, D. Y. Chirgadze, K. W. Miller, A. R. Aricescu, Differential assembly diversifies $GABA_A$ receptor structures and signalling. *Nature* **604**, 190–194 (2022).
17. J. Hénin, T. Lelièvre, M. R. Shirts, O. Valsson, L. Delemotte, Enhanced sampling methods for molecular dynamics simulations. *Living J. Comput. Mol. Sci.* **4**, 1583 (2022).
18. M. A. Cruz, T. E. Frederick, U. L. Mallimadugula, S. Singh, N. Vithani, M. I. Zimmerman, J. R. Porter, K. E. Moeder, G. K. Amarasinghe, G. R. Bowman, A cryptic pocket in Ebola VP35 allosterically controls RNA binding. *Nat. Commun.* **13**, 2269 (2022).
19. J. B. Behring, S. van der Post, A. D. Mooradian, M. J. Egan, M. I. Zimmerman, J. L. Clements, G. R. Bowman, J. M. Held, Spatial and temporal alterations in protein structure by EGF regulate cryptic cysteine oxidation. *Sci. Signal.* **13**, eaay7315 (2020).
20. B. Selvam, S. Mittal, D. Shukla, Free energy landscape of the complete transport cycle in a key bacterial transporter. *ACS Cent. Sci.* **4**, 1146–1154 (2018).
21. M. I. Zimmerman, G. R. Bowman, FAST conformational searches by balancing exploration/exploitation trade-offs. *J. Chem. Theory Comput.* **11**, 5747–5757 (2015).
22. M. Zimmerman, J. Porter, M. Ward, S. Singh, N. Vithani, A. Meller, U. Mallimadugula, C. Kuhn, J. Borowsky, R. Wiewiora, M. Hurley, A. Harbison, C. Fogarty, J. Coffland, E. Fadda, V. Voelz, J. Chodera, G. Bowman, SARS-CoV-2 simulations go exascale to predict dramatic spike opening and cryptic pockets across the proteome. *Nat. Chem.* **13**, 651–659 (2021).
23. A. B. Everitt, T. Luu, B. Cromer, M. L. Tierney, B. Birnir, R. W. Olsen, P. W. Gage, Conductance of recombinant GABA channels is increased in cells co-expressing $GABA_A$ receptor-associated protein. *J. Biol. Chem.* **279**, 21701–21706 (2004).
24. G. Pérez-Hernández, F. Paul, T. Giorgino, G. De Fabritiis, F. Noé, Identification of slow molecular order parameters for Markov model construction. *J. Chem. Phys.* **139**, 015102 (2013).
25. A. L. Germann, S. R. Pierce, A. B. Burbridge, J. H. Steinbach, G. Akk, Steady-state activation and modulation of the concatemeric $\alpha1\beta2\gamma2l$ $GABA_A$ receptor. *Mol. Pharmacol.* **96**, 320–329 (2019).
26. V. Lindahl, P. Gourdon, M. Andersson, B. Hess, Permeability and ammonia selectivity in aquaporin TIP2; 1: Linking structure to function. *Sci. Rep.* **8**, 2995 (2018).
27. P. Metzner, C. Schütte, E. Vanden-Eijnden, Transition path theory for Markov jump processes. *Multiscale Model. Simul.* **7**, 1192–1219 (2009).
28. D. del Alamo, D. Sala, H. S. Mchaourab, J. Meiler, Sampling alternative conformational states of transporters and receptors with AlphaFold2. *eLife* **11**, e75751 (2022).
29. A. Meller, S. Bhakat, S. Solieva, G. R. Bowman, Accelerating cryptic pocket discovery using AlphaFold. *J. Chem. Theory Comput.* **19**, 4355–4363 (2023).
30. G. Monteiro da Silva, J. Y. Cui, D. C. Dalgarno, G. P. Lisi, B. M. Rubenstein, High-throughput prediction of protein conformational distributions with subsampled AlphaFold2. *Nat. Commun.* **15**, 2464 (2024).
31. J. Yu, H. Zhu, R. Lape, T. Greiner, J. Du, W. Lü, L. Sivilotti, E. Gouaux, Mechanism of gating and partial agonist action in the glycine receptor. *Cell* **184**, 957–968.e21 (2021).
32. C. M. Noviello, A. Gharpure, N. Mukhtasimova, R. Cabuco, L. Baxter, D. Borek, S. M. Sine, R. E. Hibbs, Structure and gating mechanism of the $\alpha7$ nicotinic acetylcholine receptor. *Cell* **184**, 2121–2134.e13 (2021).
33. B. Lev, S. Murail, F. Poitevin, B. A. Cromer, M. Baaden, M. Delarue, T. W. Allen, String method solution of the gating pathways for a pentameric ligand-gated ion channel. *Proc. Natl. Acad. Sci. U.S.A.* **114**, E4158–E4167 (2017).
34. S. M. Burke, M. Avstrikova, C. M. Noviello, N. Mukhtasimova, J.-P. Changeux, G. A. Thakur, S. M. Sine, M. Cecchini, R. E. Hibbs, Structural mechanisms of $\alpha7$ nicotinic receptor allosteric modulation and activation. *Cell* **187**, 1160–1176.e21 (2024).
35. S. Jo, T. Kim, V. G. Iyer, W. Im, CHARMM-GUI: A web-based graphical user interface for CHARMM. *J. Comput. Chem.* **29**, 1859–1865 (2008).
36. H. I. Ingólfsson, T. S. Carpenter, H. Bhatia, P.-T. Bremer, S. J. Marrink, F. C. Lightstone, Computational lipidomics of the neuronal plasma membrane. *Biophys. J.* **113**, 2271–2280 (2017).
37. W. L. Jorgensen, J. Chandrasekhar, J. D. Madura, R. W. Impey, M. L. Klein, Comparison of simple potential functions for simulating liquid water. *J. Chem. Phys.* **79**, 926–935 (1983).
38. G. Licari, S. Dehghani-Ghahnaviyeh, E. Tajkhorshid, Membrane mixer: A toolkit for efficient shuffling of lipids in heterogeneous biological membranes. *J. Chem. Inf. Model.* **62**, 986–996 (2022).
39. W. Humphrey, A. Dalke, K. Schulten, VMD: Visual molecular dynamics. *J. Mol. Graph.* **14**, 33–38 (1996).
40. X. Huang, G. R. Bowman, S. Bacallado, V. S. Pande, Rapid equilibrium sampling initiated from nonequilibrium data. *Proc. Natl. Acad. Sci. U.S.A.* **106**, 19765–19769 (2009).
41. G. R. Bowman, V. S. Pande, F. Noé, *An Introduction to Markov State Models and Their Application to Long Timescale Molecular Simulation* (Springer Science & Business Media, vol. 797, 2013).
42. F. Noé, C. Schütte, E. Vanden-Eijnden, L. Reich, T. R. Weikl, Constructing the equilibrium ensemble of folding pathways from short off-equilibrium simulations. *Proc. Natl. Acad. Sci. U.S.A.* **106**, 19011–19016 (2009).
43. M. K. Scherer, B. Trendelkamp-Schroer, F. Paul, G. Pérez-Hernández, M. Hoffmann, N. Plattner, C. Wehmeyer, J.-H. Prinz, F. Noé, PyEMMA 2: A software package for estimation, validation, and analysis of Markov models. *J. Chem. Theory Comput.* **11**, 5525–5542 (2015).
44. C. R. Schwantes, D. Shukla, V. S. Pande, Markov state models and tICA reveal a nonnative folding nucleus in simulations of NuG2. *Biophys. J.* **110**, 1716–1719 (2016).
45. C. R. Schwantes, V. S. Pande, Improvements in Markov state model construction reveal many non-native interactions in the folding of NTL9. *J. Chem. Theory Comput.* **9**, 2000–2009 (2013).
46. E. Lyman, D. M. Zuckerman, On the structural convergence of biomolecular simulations by determination of the effective sample size. *J. Phys. Chem. B* **111**, 12876–12882 (2007).
47. H. Wu, F. Noé, Variational approach for learning Markov processes from time series data. *J. Nonlinear Sci.* **30**, 23–66 (2020).
48. J.-H. Prinz, H. Wu, M. Sarich, B. Keller, M. Senne, M. Held, J. D. Chodera, C. Schütte, F. Noé, Markov models of molecular kinetics: Generation and validation. *J. Chem. Phys.* **134**, 174105 (2011).
49. S. Páll, A. Zhmurov, P. Bauer, M. Abraham, M. Lundborg, A. Gray, B. Hess, E. Lindahl, Heterogeneous parallelization and acceleration of molecular dynamics simulations in GROMACS. *J. Chem. Phys.* **153**, 134110 (2020).
50. J. Huang, S. Rauscher, G. Nawrocki, T. Ran, M. Feig, B. L. De Groot, H. Grubmüller, A. D. MacKerell, CHARMM36m: An improved force field for folded and intrinsically disordered proteins. *Nat. Methods* **14**, 71–73 (2017).
51. J. B. Klauda, R. M. Venable, J. A. Freites, J. W. O'Connor, D. J. Tobias, C. Mondragon-Ramirez, I. Vorobyov, A. D. MacKerell, R. W. Pastor, Update of the CHARMM all-atom additive force field for lipids: Validation on six lipid types. *J. Phys. Chem. B* **114**, 7830–7843 (2010).
52. K. Vanommeslaeghe, E. P. Raman, A. D. MacKerell Jr., Automation of the CHARMM general force field (CGenFF) II: Assignment of bonded parameters and partial atomic charges. *J. Chem. Inf. Model.* **52**, 3155–3168 (2012).

53. K. Vanommeslaeghe, E. Hatcher, C. Acharya, S. Kundu, S. Zhong, J. Shim, E. Darian, O. Guvench, P. Lopes, I. Vorobyov, A. D. Mackerell, CHARMM general force field: A force field for drug-like molecules compatible with the CHARMM all-atom additive biological force fields. *J. Comput. Chem.* **31**, 671–690 (2010).
54. K. Vanommeslaeghe, A. D. MacKerell Jr., Automation of the CHARMM general force field (CGenFF) I: Bond perception and atom typing. *J. Chem. Inf. Model.* **52**, 3144–3154 (2012).
55. H. Liu, H. Fu, C. Chipot, X. Shao, W. Cai, Accuracy of alternate nonpolarizable force fields for the determination of protein-ligand binding affinities dominated by cation-π interactions. *J. Chem. Theory Comput.* **17**, 3908–3915 (2021).
56. T. Darden, D. York, L. Pedersen, Particle mesh Ewald: An *N*·log(*N*) method for Ewald sums in large systems. *J. Chem. Phys.* **98**, 10089–10092 (1993).
57. M. Parrinello, A. Rahman, Crystal structure and pair potentials: A molecular-dynamics study. *Phys. Rev. Lett.* **45**, 1196–1199 (1980).
58. G. Bussi, D. Donadio, M. Parrinello, Canonical sampling through velocity rescaling. *J. Chem. Phys.* **126**, 014101 (2007).
59. R. Evans, M. O'Neill, A. Pritzel, N. Antropova, A. Senior, T. Green, A. Žídek, R. Bates, S. Blackwell, J. Yim, O. Ronneberger, S. Bodenstein, M. Zielinski, A. Bridgland, A. Potapenko, A. Cowie, K. Tunyasuvunakool, R. Jain, E. Clancy, P. Kohli, J. Jumper, D. Hassabis, Protein complex prediction with AlphaFold-Multimer. bioRxiv 2021.10.04.463034 [Preprint] (2022). https://doi.org/10.1101/2021.10.04.463034.
60. M. Mirdita, K. Schütze, Y. Moriwaki, L. Heo, S. Ovchinnikov, M. Steinegger, ColabFold: Making protein folding accessible to all. *Nat. Methods* **19**, 679–682 (2022).
61. M. Steinegger, J. Söding, MMseqs2 enables sensitive protein sequence searching for the analysis of massive data sets. *Nat. Biotechnol.* **35**, 1026–1028 (2017).
62. W. L. DeLano, PyMOL: An open-source molecular graphics tool. *CCP4 Newslett. Protein Crystallogr.* **40**, 82–92 (2002).
63. O. S. Smart, J. G. Neduvelil, X. Wang, B. Wallace, M. S. Sansom, HOLE: A program for the analysis of the pore dimensions of ion channel structural models. *J. Mol. Graph.* **14**, 354–360 (1996).
64. W. Chojnacka, J. Teng, J. J. Kim, A. A. Jensen, R. E. Hibbs, Structural insights into $GABA_A$ receptor potentiation by quaalude. *Nat. Commun.* **15**, 5244 (2024).
65. G. Klesse, S. Rao, M. S. Sansom, S. J. Tucker, CHAP: A versatile tool for the structural and functional annotation of ion channel pores. *J. Mol. Biol.* **431**, 3353–3365 (2019).
66. S. Zhu, A. Sridhar, J. Teng, R. J. Howard, E. Lindahl, R. E. Hibbs, Structural and dynamic mechanisms of $GABA_A$ receptor modulators with opposing activities. *Nat. Commun.* **13**, 4582 (2022).

Acknowledgments: We thank M. Zimmerman, R. Hibbs, W. Chojnacka, and the Molecular Biophysics Stockholm environment for valuable feedback and discussion. MD simulations were performed using computing facilities of the Karolina, LUMI, and Discoverer supercomputers through the European High Performance Computing Joint Undertaking (EuroHPC) and through the Swedish National Infrastructure for Computing (SNIC) supported by BioExcel. S.E.L. was further supported by the Sven and Lilly Lawski Foundation and R.J.H. and E.L. by the Swedish e-Science Research Center (SeRC). **Funding:** This work was supported by EuroHPC grants EHPC-REG-2023R01-103, EHPC-REG-2022R03-223, and EHPC-REG-2022R03-219 (N.H.), EuroHPC BioExcel grant 101093290 (E.L.), Marie Sklodowska-Curie Postdoctoral Fellowship grant 101107036 (N.H.), SNIC grant 2022/3-40 (E.L.), and Swedish Research Council (VR) grants 2019-02433 and 2021-05806 (R.J.H. and E.L.). **Author contributions:** Research design, performing simulations, and data analysis: N.H. AF calculations: S.E.L. Writing: N.H., R.J.H., and E.L. Editing: N.H., S.E.L., R.J.H., and E.L. Conceptualization: N.H. Data curation: N.H. and R.J.H. Formal analysis: N.H. Funding acquisition: N.H., S.E.L., and E.L. Investigation: N.H. Methodology: N.H. and S.E.L. Project administration: R.J.H. and E.L. Resources: N.H. and E.L. Software: N.H. Supervision: R.J.H. and E.L. Validation: N.H. Visualization: N.H. Writing—original draft: N.H. Writing—review and editing: N.H., S.E.L., R.J.H., and E.L. **Competing interests:** The authors declare that they have no competing interests. **Data and materials availability:** All data needed to evaluate the conclusions in the paper are present in the paper and/or the Supplementary Materials. The raw MD simulation trajectories can be found on Zenodo (DOI: 10.5281/zenodo.10964268).

Submitted 10 May 2024
Accepted 4 December 2024
Published 8 January 2025
10.1126/sciadv.adq3788